ACTA METALLURGICA SLOVACA
2022, VOL. 28, NO. 1, 33-42

RESEARCH PAPER

THE INFLUENCE OF CHEMICAL COMPOSITION ON THE PHASE BALANCE, MICROSTRUCTURE, HIGH-TEMPERATURE STRENGTH AND FRACTURE TOUGHNESS OF Ti–Si–X AND Ti–Cr–X COMPOSITES

Volodymyr Kulyk[1], Bogdan Vasyliv[2], Zoia Duriagina[1,3], Pavlo Lyutyy[1], Valentyna Vavrukh[1], Taras Kovbasiuk[1], Volodymyr Vira[4], Myroslav Holovchuk[5], Tetiana Loskutova[6]*

[1]*Department of Materials Science and Engineering, Lviv Polytechnic National University, Lviv, S. Bandera str. 12, 79013, Ukraine*
[2]*Department of Hydrogen Technologies and Alternative Energy Materials, Karpenko Physico-Mechanical Institute of the NAS of Ukraine, Lviv, Naukova str. 5, 79060, Ukraine*
[3]*The John Paul II Catholic University of Lublin, Al. Racławickie 14, 20-950 Lublin, Poland*
[4]*Department of Strength of Materials and Structural Mechanics, Lviv Polytechnic National University, Lviv, S. Bandera str. 12, 79013, Ukraine*
[5]*Department of Corrosion and Corrosion Protection, Karpenko Physico-Mechanical Institute of the NAS of Ukraine, Lviv, Naukova str. 5, 79060, Ukraine*
[6]*Department of Materials Science and Heat Treatment, National Technical University of Ukraine "Igor Sikorsky Kyiv Polytechnic Institute", Kyiv, Peremohy ave. 37, 03056, Ukraine*

*Corresponding author: kulykvolodymyrvolodymyrovych@gmail.com, tel.: +380672823572, Department of Materials Science and Engineering, Lviv Polytechnic National University, Lviv, 79013, Ukraine

Received: 10.01.2022
Accepted: 03.02.2022

ABSTRACT

Advanced Ti-based composites possess a high strength-to-weight ratio and fracture toughness in a temperature range 20–650 °C and show a potential for applications in components of up-to-date internal combustion and aircraft engines and equipment for power generation (fuel cells, gas turbines, compressors, etc.). However, to meet the requirements on the high-temperature reliability of the products for critical engineering, the operating temperature of developed Ti-based composites should be increased to 750−800 °C. In this work, composites of Ti–Si–X (X=Al and/or Sn, Zr, C) and Ti–Cr–X (X=Al and/or C) systems have been studied. Series of beam specimens were manufactured by casting. A part of cast specimens was undergone to thermo-mechanical deformation. A strength test of specimens was carried out according to a three-point bend scheme in a temperature range 20–1000 °C. A single-edge notch beam (SENB) test of specimens was conducted according to the same scheme in a temperature range 20–900 °C and fracture toughness of materials was estimated. General trends in high-temperature strength and fracture toughness of the studied composites were substantiated in terms of morphology of the microstructural components and fracture micromechanisms, and the effect of alloying with ultrafine elements on resulting mechanical characteristics of the studied composites was found.

Keywords: Ti–Si–X and Ti–Cr–X composites; MAX phase; high-temperature strength; fracture toughness; phase composition; microstructure; fracture micromechanism

INTRODUCTION

To ensure required operating life of parts and products in hard operating conditions, there is a need to use high-strength and oxidation-resistant materials like advanced ceramics (zirconia, alumina, silicon nitride, silicon carbide, etc.) and various composites. These materials have excellent high-temperature strength and chemical inertness and can operate under high pressure or vacuum, high temperature, radiation, corrosion, etc. [1–10].

State-of-the-art Ti-based composites possessing high strength and fracture toughness in a temperature range 20–650 °C have an advantage over traditional cast or deformed titanium alloys, for which an operating temperature is limited by 350–450 °C. Such Ti-based composites possess a high strength-to-weight ratio and show a potential for applications in components of up-to-date internal combustion and aircraft engines and equipment for power generation (fuel cells, gas turbines, compressors, etc.) [11–22]. However, to meet the requirements on the high-temperature reliability of the products for critical engineering, the operating temperature of developed Ti-based composites should be increased to 750−800 °C. Under such conditions, these materials must maintain high strength and crack growth resistance as well as corrosion resistance [11, 23–25]. This should be taken into account while developing new ceramics and composites as well as modifying microstructure and improving mechanical characteristics of known materials [26–33]. The substantiation of chemical composition and processing and treatment modes are crucial issues in improving the phase compositions, microstructure, and mechanical properties of the developed materials [34–43].

Depending on the chemical composition, Ti and Cr based composites may comprise some amount of high-temperature phases, namely, silicides, aluminides, MAX phases, etc. [44–51]. In particular, MAX phases are formed as quite distinct regions along the boundaries of titanium or chromium grains in Ti and Cr based composites [52–55]. It was shown in a number of works that MAX phases may be effectively used in aerospace industry and mechanical engineering as well as in power generation equipment [2, 54, 56]. MAX phases are ternary compounds which can be described by the conditional formula $M_{n+1}AX_n$ (n = 1, 2, 3 …). In this formula, M corresponds to a transition metal of the *d*-group (Sc, Ti, V, Cr, Zr, Nb, Mo, Hf, Ta), whereas A corresponds to an element of the *p*-group (Si, Ge, Al, Ga, S, P, Sn, As, Cd, I, Tl, Pb) and X corresponds to carbon or nitrogen [57].

Among a variety of MAX phases, Ti_3SiC_2 MAX phase does not demonstrate perfect self-healing performance. In the case when the A atoms of Ti_3SiC_2 are partially replaced with Al, $Ti_3Si_{1-x}Al_xC_2$ solid solutions are formed [18,52,58] that improves self-healing performance of the material due to the rapid diffusion and oxidation of aluminum and a high oxidation resistance of aluminum oxide. Besides, the oxidation temperature of Al can be lowered to 900 °C in the case of partial replacement of Al with Sn in Ti_2AlC MAX phase [18, 49, 52, 59]. At temperatures below 600 °C, SnO_2 can be already formed in $Ti_2Al_{1-x}Sn_xC$ providing its good crack filling properties in this temperature range. However, no significant increase in the mechanical strength was found in such a composite because of the low mechanical strength of a SnO_2 compound and the low bond strength [52, 59, 60].

It is known that MAX phases are among a variety of compounds which belong to the hexagonal crystal system [51, 52, 57, 58]. This peculiarity allows using HP and SPS techniques of pressure-assisted sintering for manufacturing textured bulk MAX phases. As a result, the material consists of plate-like grains preferentially oriented under external conditions (e.g., a magnetic field or a uniaxial pressure). In addition to the mentioned fabrication techniques, spark plasma sintering or direct hot pressing of MAX phases not allowing formation of highly textured material, still may result in formation comparatively distinct MAX phase regions along the boundaries of titanium grains in Ti and Cr based composites [13,52,61–65].

It is also known about an anisotropy of mechanical properties of bulk MAX phases. In particular, high crack growth resistance and mechanical strength of these materials along specific directions may be attributed to the lamellar crystal structure [52, 57]. Such mechanical behavior makes them attractive for applications in hard operating conditions.

Wear resistance and strength tests of ceramics and composites are widely used for estimating the bearing capacity of the corresponding products [54, 66–68]. However, to prevent the degradation of microstructure of materials in environmentally assisted harsh conditions [69–73], there is a need to obtain material resistive to microstructural changes in such conditions [74–77]. Microhardness and fracture toughness serve as characteristics of material for estimating its resistance to the nucleation and growth of microcracks. For this purpose, the indentation test as one of the simplest known mechanical method is used [66, 78, 79]. Based on the indentation technique, a variety of loading schemes and formulas for calculating fracture toughness of materials were proposed [69, 78, 80, 81]. Thus, to develop a new ceramic or composite material with required physical and mechanical properties, it should be studied in terms of strength and crack growth resistance and their relations to the chemical and phase compositions.

The work is aimed at evaluating the influence of chemical composition on the phase balance, microstructure, high-temperature fracture toughness and strength, as well as fracture micromechanisms of Ti–Si–X and Ti–Cr–X composites.

MATERIAL AND METHODS

In this work, titanium-based composites of various systems have been studied. The composites were prepared from raw materials by arc melting in an argon atmosphere on a water-cooled copper hearth [54, 61]. The purities of the elements were as follows: Ti > 99.6 at%; Cr > 99.99 at%; and Si, C, Al, Sn, Zr > 99.99 at%. After melting, ingots were annealed at 1200 °C for 5 min. In some cases (composites 2 and 3, Table 1), ingots were rolled at a temperature of 1050 °C with applying of the thermo-mechanical deformation of about 40%.

Beam specimens 5.0×7.5×50 mm in size were machined from ingots or blanks, grinded, and polished (**Table 1**).

Table 1 Types of the investigated composites and their marking

Composite marking	System
1	Ti–Si–Al–Sn–C
2	Ti–Si–Al–Zr–C
3	Ti–Si–Al–Zr–C
4	Ti–Cr–Al–C

The specimens were tested according to a three-point bend scheme in a temperature range 20–1000 °C. Based on the "load–flexure" dependences, the fracture stress (σ_f) was calculated by the following equation [24,31,35,75]:

$$\sigma_f = \frac{1.5 \cdot P \cdot S}{b \cdot t^2} \quad (1.)$$

where P is the peak load, S is the distance between supporting rollers, b is the specimen width, and t is the specimen thickness. To characterize crack growth resistance of materials [82–86], a fracture toughness characteristic, namely, the critical stress intensity factor (SIF) K_{Ic} is often used. One of the simplest methods of estimation of the fracture toughness is an indentation method implementing a variety of formulas for calculating the SIF [87–96]. For a lot of materials, the K_{Ic} values calculated by some of these formulas are consistent with those obtained by conventional methods of fracture mechanics [78, 96, 97]. Among the last ones, a single-edge notch beam (SENB) test [98–100] is widely used to estimate fracture toughness of ceramic and composite materials. This method was thoroughly described in [97].

In our work, we conducted fracture toughness tests using the mentioned SENB test method. Specimen series were investigated in a temperature range 20–900 °C using a three-point bend scheme. For estimating the critical SIF of materials corresponding formulas [98–100] were used.

At least 3 specimens were used for each test temperature of corresponding test methods.

For the study of fracture surface morphology and microstructure of specimens we used a scanning electron microscope (SEM) Carl Zeiss EVO-40XVP. An INCA Energy 350 system was used for an energy-dispersive X-ray (EDX) microanalysis of chemical composition of the materials both in secondary electron (SE) and back-scattered electron (BSE) imaging modes.

X-ray diffraction (XRD) patterns were recorded on an X-ray diffractometer (Aeris, Malvern Panalytical, United Kingdom) with Cu Kα radiation operating at 40 kV and 15 mA in the angular range 2θ of 20–90°, with a step of 0.0217°. The XRD analysis was perfomed using Highscore software and referenced with the International Center for Diffraction Data (ICDD). The procedures of indexing and structure solutions, as well as the profile

and structural parameters refinements were carried out using the WinCSD [101] program.

RESULTS AND DISCUSSION

The microstructure and mechanical properties of the titanium-based composites of Ti–Si–X and Ti–Cr–X systems in a wide temperature range have been studied.

XRD analysis of the studied composites

Ti–Si–Al–Sn–C composite (1). The XRD patterns of the investigated composites (**Fig. 1**) show in detail the peculiarities of their phase balances. The XRD pattern of composite 1 (Ti–Si–Al–Sn–C system) contains only peaks of the α-Ti and $TiC_{0.67}$ phases (Fig. 1a).

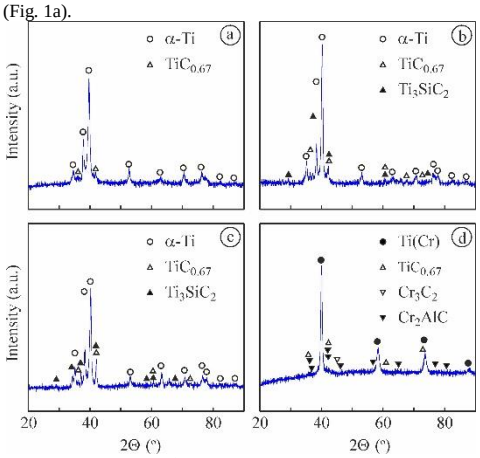

Fig. 1 XRD patterns of the investigated composites (a) 1, (b) 2, (c) 3, and (d) 4 (see Table 1)

The α-Ti phase percentage was found to be about 90 wt%, whereas the $TiC_{0.67}$ phase percentage was about 10 wt%. The morphology of these phases was investigated in details using the microstructure images made at various magnifications. At a low magnification, one can see quite homogeneous microstructure of the Ti–Si–Al–Sn–C composite (**Fig. 2a**). At a higher magnification, we can observe distinct microstructural components of this composite (**Fig. 2b**). According to a general EDX analysis (spectrum 1 in **Fig. 2b** and **Table 2**), this material contains 87.41 wt% Ti, 6.09 wt% Al, 3.15 wt% Si, and 3.35 wt% Sn. The results of EDX analysis showed some difference in chemical composition of the Ti–Si–Al–Sn–C composite material as compared to the results of XRD analysis. According to EDX analysis (**Fig. 2b** and **Table 2**), this material is a metal-matrix composite of Ti–Si–Al–Sn–C system with high titanium content. It possibly comprises the titanium matrix phase, Ti_5Si_3 phase [54, 56, 61], Ti_3SiC_2 MAX phase, and titanium carbide phase. EDX mapping (Fig. 3) shows locations of chemical elements and can be a useful tool for detecting these phases.

The titanium phase (α-Ti of about 87 wt% Ti, spectrum 2 in Fig. 2b and Table 2) with some amounts of aluminum (6.26 wt%), silicon (2.39 wt%), and tin (3.88 wt%) is a matrix phase. The total amount of the α-Ti phase estimated optically using the microstructure image (Fig. 2b) according to a technique [7] is about 66–70 vol%.

The Ti_5Si_3 phase with small amounts of aluminum (4.35 wt%) and tin (2.2 wt%) looks like thin elongated curved areas of light-gray color about 25 μm in length (spectrum 3 in **Fig. 2b**). These areas are located at the boundaries of titanium lamella packets. The total area occupied by them (Fig. 2b) is about 11–12 vol%. The Ti_5Si_3 phase was not detected by XRD analysis because of its low percentage.

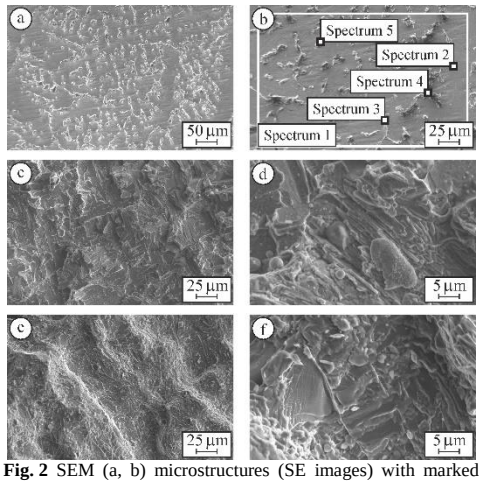

Fig. 2 SEM (a, b) microstructures (SE images) with marked zones of (b) general (spectrum 1) and local (spectra 2, 3, 4, and 5) EDX analyses, and (c, d, e, f) fractography (SE images) of specimens of composite 1 after fracture toughness tests at (c, d) 20 °C and (e, f) 650 °C (Table 1)

Table 2 The data of the EDX spectra 1–5 marked in Fig. 2 for a specimen of composite 1 (Table 1)

Chemical element and X-ray series	Spectra 1		2		3		4		5	
	wt%	at%	wt%	at%	wt%	at%	wt%	at%	wt%	at%
C K	–	–	–	–	–	–	14.88	38.85	24.62	54.32
Al K	6.09	10.31	6.26	10.66	4.35	6.98	3.25	3.77	2.74	2.69
Si K	3.15	5.12	2.39	3.92	12.44	19.14	9.87	11.04	9.68	9.13
Ti K	87.41	83.28	87.47	83.92	81.01	73.08	69.95	45.80	59.80	33.08
Fe K	–	–	–	–	–	–	–	–	0.21	0.10
Cd L	–	–	–	–	–	–	–	–	1.31	0.31
Sn L	3.35	1.29	3.88	1.50	2.20	0.80	2.05	0.54	1.64	0.37

The Ti_3SiC_2 MAX phase with small amounts of aluminum (3.25 wt%) and tin (2.05 wt%) looks like thick elongated areas of dark-gray color about 15 μm in size (spectrum 4 in Fig. 2b). These areas are located at the boundaries of titanium lamella packets similarly to the Ti_5Si_3 phase. Carbon in these areas was detected by EDX mapping (Fig. 3e). The total amount of the MAX phase (Fig. 2b) is about 14–15 vol%. Both the Ti_5Si_3 phase and the Ti_3SiC_2 MAX phase were not detected by XRD analysis because of their low percentages.

The titanium carbide phase ($TiC_{0.67}$, spectrum 5 in Fig. 2b) is in the form of distinct round-shaped particles of dark-gray color about 3 μm in size. The particles are distributed uniformly both in the α-Ti matrix phase and at the boundaries of titanium lamella packets. Similarly to the Ti_3SiC_2 MAX phase, the presence of carbon in these places was revealed by EDX mapping (Fig. 3e). The total area occupied by them (Fig. 2b) is about 5–7 vol%. Besides, small amounts of the Ti_5Si_3 phase and the Ti_3SiC_2 MAX phase are probably neighboring these carbide phase particles since some amount of silicon (9.68 wt%), along with small amounts of aluminum (2.74 wt%), iron (0.21 wt%), cadmium (1.31 wt%), and tin (1.64 wt%), were also detected in these areas.

Ti–Si–Al–Zr–C composite (2). The XRD pattern of composite 2 (Ti–Si–Al–Zr–C system) contains peaks of the α-Ti, $TiC_{0.67}$, and Ti_3SiC_2 MAX phases (Fig. 1b). Its phase composition was found to be as follows: α-Ti phase (about 70 wt%), $TiC_{0.67}$ phase (about

12 wt%), and Ti_3SiC_2 MAX phase (about 18 wt%). The microstructure image of the Ti–Si–Al–Zr–C composite made at a low magnification showed its homogeneous microstructure (**Fig. 4a**). The microstructure image of a higher magnification presents uniformly distributed areas of arbitrary shapes differing in colors (**Fig. 4b**). A general EDX analysis (spectrum 1 in **Fig. 4b** and **Table 3**) showed 76.79 wt% Ti, 6.77 wt% C, 3.88 wt% Al, 5.75 wt% Si, and 6.81 wt% Zr in this material. Thus, this material is a metal-matrix composite of Ti–Si–Al–Zr–C system possibly comprising the titanium matrix phase, $(Ti, Zr)_5Si_3$ phase [54, 56, 61], Ti_3SiC_2 MAX phase, and titanium carbide phase. Locations of these phases may be determined using EDX mapping **(Fig. 5**).

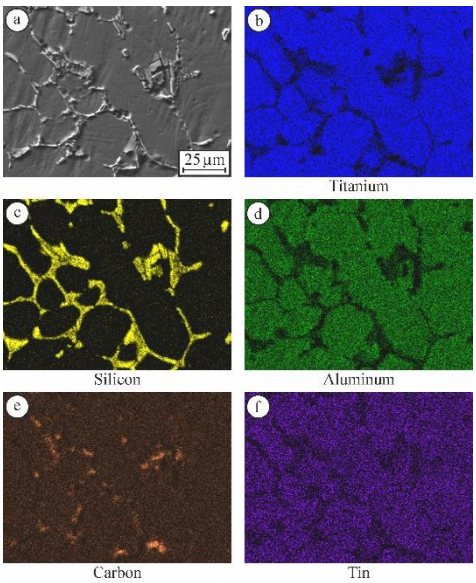

Fig. 3 SEM microstructure of composite 1 (a) and related EDX maps of (b) titanium, (c) silicon, (d) aluminum, (e) carbon, and (f) tin

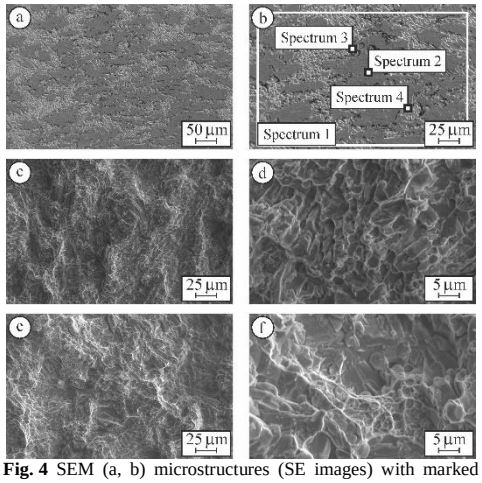

Fig. 4 SEM (a, b) microstructures (SE images) with marked zones of (b) general (spectrum 1) and local (spectra 2, 3, and 4) EDX analyses, and (c, d, e, f) fractography (SE images) of specimens of composite 2 after fracture toughness tests at (c, d) 20 °C and (e, f) 700 °C (**Table 1**)

The α-Ti phase (89.65 wt% Ti, spectrum 2 in **Fig. 4b** and Table 3) with some amounts of aluminum (5.14 wt%), silicon (1.1 wt%), and zirconium (4.11 wt%) is a matrix phase. The total amount of the α-Ti phase (**Fig. 4b**) is about 52–55 vol%.

The $(Ti, Zr)_5Si_3$ phase looks like round-shaped particles of dark-gray color about 5 µm in size (spectrum 3 in **Fig. 4b**). These areas are adjacent to the titanium lamella packets. The total area occupied by them (**Fig. 4b**) is about 4–6 vol%. Besides, small amounts of the Ti_3SiC_2 MAX phase and the $TiC_{0.67}$ phase are probably neighboring these particles since some amount of carbon (6.97 wt%),

along with a small amount of aluminum (1.46 wt%), was also detected in these areas. However, the $(Ti, Zr)_5Si_3$ phase was not revealed by XRD analysis because of its small percentage.

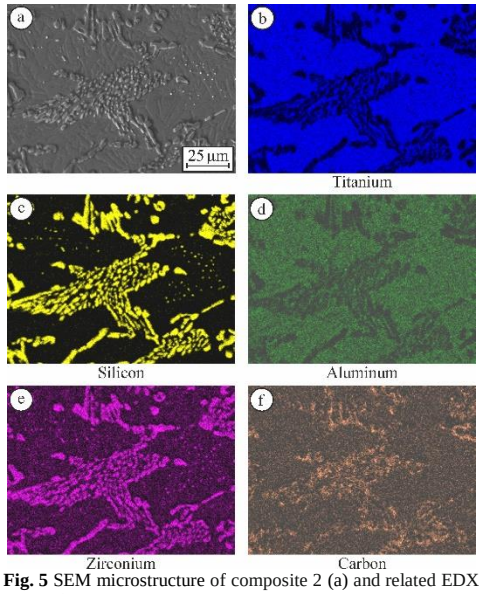

Fig. 5 SEM microstructure of composite 2 (a) and related EDX maps of (b) titanium, (c) silicon, (d) aluminum, (e) zirconium, and (f) carbon

The titanium carbide phase $TiC_{0.67}$ with small amount of the Ti_3SiC_2 MAX phase and also small amounts of aluminum (5.09 wt%) and zirconium (2.69 wt%) looks like textured bulk MAX phase regions about 35–60 µm in size consisting of thin lamellae (spectrum 4 in **Fig. 4b**). These regions are uniformly distributed in the titanium matrix. The total amount of these regions (**Fig. 4b**) is about 35–45 vol%.

Table 3 The data of the EDX spectra 1–4 marked in Fig. 4 for a specimen of composite 2 (Table 1)

Chemical element and X-ray series	Spectra 1		2		3		4	
	wt%	at%	wt%	at%	wt%	at%	wt%	at%
C K	6.77	21.75	–	–	6.97	21.55	7.30	22.94
Al K	3.88	5.56	5.14	8.88	1.46	2.01	3.07	4.29
Si K	5.75	7.91	1.10	1.82	19.69	26.04	10.62	14.26
Ti K	76.79	61.90	89.65	87.20	57.46	44.53	69.10	54.41
Zr L	6.81	2.88	4.11	2.10	14.42	5.87	9.91	4.10

Ti–Si–Al–Zr–C composite (3). The XRD pattern of composite 3 (Ti–Si–Al–Zr–C system) is similar to that of composite 2 and contains peaks of the α-Ti, $TiC_{0.67}$, and Ti_3SiC_2 MAX phases (**Fig. 1c**). Its phase composition is as follows: α-Ti phase (about 75 wt%), $TiC_{0.67}$ phase (about 17 wt%), and Ti_3SiC_2 MAX phase (about 8 wt%). The microstructure image of the Ti–Si–Al–Zr–C composite made at a low magnification showed a quite homogeneous microstructure with some resemblance to the microstructure of composite 2 (**Fig. 6a**). The microstructure image of a higher magnification presents randomly distributed areas of arbitrary shapes (**Fig. 6b**). As a result of a general EDX analysis (spectrum 1 in **Fig. 6b** and **Table 4**), 83.1 wt% Ti, 5.07 wt% Al, 5.94 wt% Si, and 5.89 wt% Zr were found in this material. Unexpectedly, no signs of carbon were detected. Like composite 2, this material is a metal-matrix composite of Ti–Si–Al–Zr–C system possibly comprising the α-Ti matrix phase, $(Ti, Zr)_5Si_3$ phase [54, 56, 61], Ti_3SiC_2 MAX phase (only according to XRD analysis), and titanium carbide phase. Locations of these phases may also be determined using EDX mapping (**Fig. 7**).

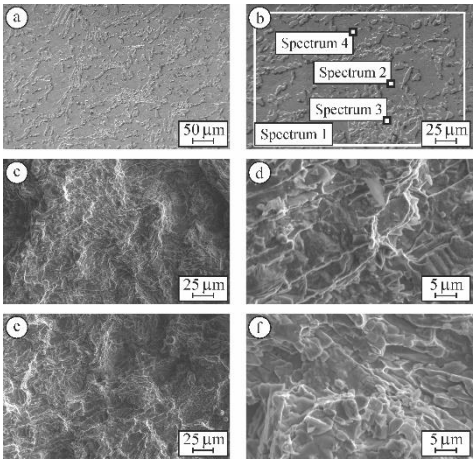

Fig. 6 SEM (a, b) microstructures (SE images) with marked zones of (b) general (spectrum 1) and local (spectra 2, 3, and 4) EDX analyses, and (c, d, e, f) fractography (SE images) of specimens of composite 3 after fracture toughness tests at (c, d) 20 °C and (e, f) 700 °C (Table 1)

The α-Ti matrix phase (89 wt% Ti, spectrum 2 in **Fig. 6b** and **Table 4**) with some amounts of aluminum (5.99 wt%), silicon (1.07 wt%), and zirconium (3.94 wt%) is presented in an amount of about 56–60 vol%.

The $(Ti, Zr)_5Si_3$ phase with a small amount of aluminum (2.07 wt%) looks like particles of arbitrary shapes about 5–25 µm in size united in colonies or distributed randomly (spectrum 3 in **Fig. 6b**). They occupy the total area of about 26–30 vol% (**Fig. 6b**). For an unknown reason, this phase was not detected by XRD analysis.

Table 4 The data of the EDX spectra 1–4 marked in Fig. 6 for a specimen of composite 3 (Table 1)

Chemical element and X-ray series	Spectra 1		2		3		4	
	wt%	at%	wt%	at%	wt%	at%	wt%	at%
C K	–	–	–	–	–	–	11.22	32.70
Al K	5.07	8.55	5.99	10.27	2.07	3.32	5.09	6.61
Si K	5.94	9.61	1.07	1.76	20.85	32.09	0.88	1.09
Ti K	83.10	78.90	89.00	85.97	65.45	59.08	80.12	58.57
Zr L	5.89	2.94	3.94	2.00	11.63	5.51	2.69	1.03

The $TiC_{0.67}$ phase with a small amount of the Ti_3SiC_2 MAX phase and some amounts of aluminum (5.09 wt%) and zirconium (2.69 wt%) looks like particles of arbitrary shapes about 1–5 µm in size distributed randomly in titanium matrix (spectrum 4 in **Fig. 6b**). The total amount of these particles (**Fig. 6b**) is about 14–18 vol%.

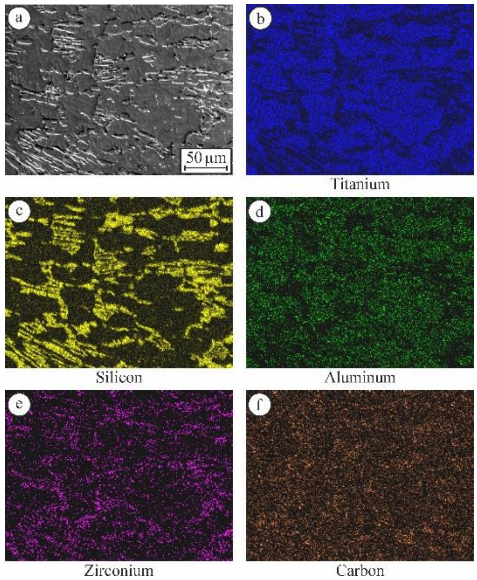

Fig. 7 SEM microstructure of composite 3 (a) and related EDX maps of (b) titanium, (c) silicon, (d) aluminum, (e) zirconium, and (f) carbon

Ti–Cr–Al–C composite (4). The XRD pattern of composite 4 (Ti–Cr–Al–C system) contains peaks of the Ti(Cr), $TiC_{0.67}$, Cr_3C_2, and Cr_2AlC phases (**Fig. 1d**). Its phase composition was found to be as follows: Ti(Cr) phase (about 78 wt%), $TiC_{0.67}$ phase (about 12 wt%), Cr_3C_2 phase (about 4 wt%), and Cr_2AlC phase (about 6 wt%). At a low magnification, distinctly grained microstructure of the Ti–Cr–Al–C composite can be observed (**Fig. 8a**). The microstructure image of a higher magnification presents grains of a matrix phase with uniformly distributed tiny particles inside and the fringe-like grain boundary regions. The fringes consist of needle-shaped particles differing in colors (**Fig. 8b**). A general EDX analysis (spectrum 1 in **Fig. 8b** and **Table 5**) showed 54.4 wt% Ti, 37.34 wt% Cr, 5.12 wt% C, and 3.14 wt% Al in this material. The material presenting a metal-matrix composite of Ti–Cr–Al–C system possibly comprises the Ti(Cr) matrix phase, chromium oxide phase, Cr_3C_2 phase, $TiC_{0.67}$ phase, and Cr_2AlC or/and $(Cr_{2/3}Ti_{1/3})_3AlC_2$ MAX phase [3,18,102]. Locations of these phases may be determined using EDX mapping (**Fig. 9**).

The Ti(Cr) matrix phase comprises titanium (57.3 wt%, spectrum 2 in **Fig. 8b** and **Table 5**) and chromium (39.2 wt%) with some amount of aluminum (3.5 wt%). The total amount of the Ti(Cr) phase (**Fig. 8b**) is about 66–72 vol%.

The areas of black color located at the grain boundaries (spectrum 3 in **Fig. 8b**) contain in total 49.17 wt% Ti, 25.14 wt% Cr, 14.3 wt% C, 8.08 wt% O, and 3.31 wt% Al. The maximum amounts of chromium and oxygen exactly at the grain boundaries (**Fig. 9c** and **Fig. 9d**, respectively) evidence a hypothesis on the existence of the chromium oxide phase in this composite

[102]. Some amounts of titanium, aluminum, and carbon detected by EDX analysis (spectrum 3 in **Fig. 8b** and **Table 5**) are presented in the surrounding Ti(Cr) matrix phase and also in tiny particles of the titanium/chromium carbide phase. The total amount of these areas (**Fig. 8b**) is about 4–6 vol%.

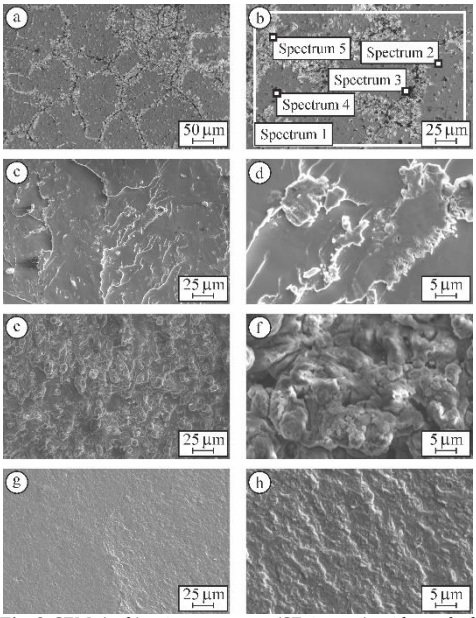

Fig. 8 SEM (a, b) microstructures (SE images) with marked zones of (b) general (spectrum 1) and local (spectra 2, 3, 4, and 5) EDX analyses, and (c, d, e, f, g, h) fractography (SE images) of specimens of composite 4 after fracture toughness tests at (c, d) 20 °C, (e, f) 700 °C, and (g, h) 800 °C (Table 1)

Table 5 The data of the EDX spectra 1–5 marked in Fig. 8 for a specimen of composite 4 (Table 1)

Chemical element and X-ray series	Spectra 1		2		3		4		5	
	wt%	at%	wt%	at%	wt%	at%	wt%	at%	wt%	at%
C K	5.12	17.78	–	–	14.30	35.77	11.99	35.30	6.29	19.95
O K	–	–	–	–	8.08	15.17	–	–	3.86	9.20
Al K	3.14	4.85	3.50	6.23	3.31	3.69	2.98	3.91	2.74	3.87
Ti K	54.40	47.40	57.30	57.52	49.17	30.84	50.98	37.63	50.29	40.00
Cr K	37.34	29.97	39.20	36.25	25.14	14.53	34.05	23.16	36.82	26.98

A local EDX analysis of a round-shaped particle of dark-gray color about 1 µm in size (spectrum 4 in **Fig. 8b** and **Table 5**) showed 50.98 wt% Ti, 34.05 wt% Cr, 11.99 wt% C, and 2.98 wt% Al. This particle probably was the titanium carbide phase $TiC_{0.67}$ or Cr_3C_2 phase identified by XRD analysis, whereas some amounts of titanium, chromium, and aluminum were detected by EDX analysis in the surrounding Ti(Cr) matrix phase. The total amount of these carbide particles was about 10–12 vol%.

The thin needle-shaped particles of light-gray color about 15 µm in length (spectrum 5 in **Fig. 8b**) forming the fringe-like grain boundary regions and containg 50.29 wt% Ti, 36.82 wt% Cr, 6.29 wt% C, 3.86 wt% O, and 2.74 wt% Al present a mixture of the $TiC_{0.67}$, Cr_2AlC or/and $(Cr_{2/3}Ti_{1/3})_3AlC_2$ MAX phase [3, 18, 102], and Al_2O_3 phases that surround the Ti(Cr) phase grains. EDX mapping shows the absence of titanium in the thin needle-shaped particles (**Fig. 9b**) and quite large amounts of chromium and aluminum (**Fig. 9c** and **Fig. 9e**, respectively). This evidences the Cr_2AlC or/and $(Cr_{2/3}Ti_{1/3})_3AlC_2$ MAX phase to be adjacent to the chromium oxide phase and located along Ti(Cr) grain boundaries as needle-shaped (textured) microregions [3,102]. In contrast, quite large amounts of oxygen and carbon can be seen on the "needle-shaped fringes–Ti(Cr) matrix" interfaces (**Fig. 9d** and **Fig. 9f**, respectively) that confirms the location of the titanium/chromium carbide phase and Al_2O_3 phase in these places. The total amount of the regions occupied by these phases is about 14–16 vol%. However, the Al_2O_3 phase was not detected by XRD analysis because of its small percentage.

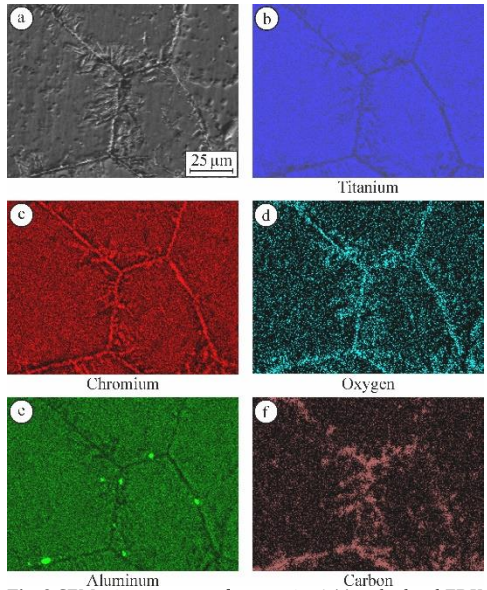

Fig. 9 SEM microstructure of composite 4 (a) and related EDX maps of (b) titanium, (c) chromium, (d) oxygen, (e) aluminum, and (f) carbon

Mechanical behavior of the studied composites and microstructure related fracture mechanisms

The studied composites exhibited distinct temperature dependences of both strength and fracture toughness (**Fig. 10**). In particular, the composites 1 (Ti–Si–Al–Sn–C system), 2 (Ti–Si–Al–Zr–C system), and 3 (Ti–Si–Al–Zr–C system) showed high and invariant values of fracture toughness (**Fig. 10b**) in a temperature range of 20 °C to 500 °C. In this range, fracture toughness of these composites is about 20 MPa·$m^{1/2}$. In contrast, the monotonously changing temperature dependences of strength (increasing for composite 1 and decreasing for composites 2 and 3, **Fig. 10a**) were revealed.

A specimen of composite 1 undergone to the fracture toughness test at 20 °C exhibited a distinct fracture surface (**Fig. 2c, d**) corresponding to a mixed fracture along the boundaries of titanium lamella packets and transgranular fracture across titanium grains in the case when a cleavage plane coincides with the direction of crack propagation. This fracture micromechanism is related to the comparatively high fracture toughness (**Fig. 10b**). Strength of this composite increased from about 760 MPa at 20 °C to 1000 MPa at 500 °C.

Fracture surface of a specimen of composite 2 tested at 20 °C (**Fig. 4c, d**) corresponds to a fracture along the boundaries of ti-

tanium lamella packets. No transgranular fracture across titanium grains occurred. Therefore, a coarse relief of fracture surface was formed that was a reason of high fracture toughness of the composite (**Fig. 10b**).

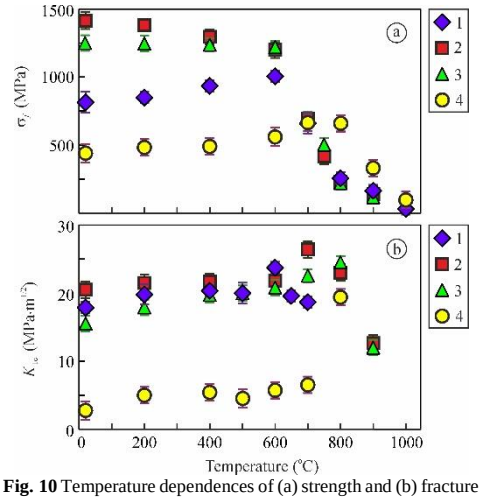

Fig. 10 Temperature dependences of (a) strength and (b) fracture toughness of the studied composites (Table 1)

Similarly to this material, fracture surface of a specimen of composite 3 tested at 20 °C (**Fig. 6c, d**) exhibited a coarse relief corresponding to high fracture toughness of the composite (**Fig. 10b**).

Strength of composites 2 and 3 decreased from 1400 MPa and 1250 MPa at 20 °C to 1230 MPa and 1240 MPa at 500 °C, respectively. Nevertheless, such a level of strength is high enough and meets the requirements to materials of this system.

A testing temperature in a range of 600 °C to 850 °C is critical for these three composites since for each composite a maximum of fracture toughness appeared on the corresponding dependence is shifted towards a certain temperature. Its location is related to the microstructural peculiarities of a composite, its chemical and phase compositions, as well as dominant fracture micromechanism.

For composite 1, a temperature above 600 °C is critical since it corresponds to the maximum of fracture toughness (**Fig. 10b**). A specimen undergone to the fracture toughness test at 650 °C exhibited blunted edges of titanium lamella packets (**Fig. 2e**), microregions of transverse fracture of thin Ti_3SiC_2 MAX phase lamellae (**Fig. 2f**), and signs of quazi-brittle failure of the Ti_5Si_3 phase grains on fracture surface (**Fig. 2f**). The fracture toughness is as high as in the case of testing at 20 °C (**Fig. 10b**). Obviously, a transition from quazi-brittle (at 600 °C) to high-temperature ductile fracture (at 650 °C) occurred that was followed by some lowering of fracture toughness (from 24 MPa·m$^{1/2}$ at 600 °C to 19 MPa·m$^{1/2}$ at 650 °C, **Fig. 10b**). Probably, tin also contributes to the transition process. Strength of this composite decreased from about 1000 MPa at 600 °C to 650 MPa at 700 °C (**Fig. 10a**).

A temperature corresponding to the maximum of fracture toughness for composite 2 is about 700 °C (**Fig. 10b**). Such a shift by 100 °C compared to composite 1 is important in terms of high-temperature mechanical stability of the studied composites. Fracture surface of a specimen of composite 2 tested at 700 °C **(Fig. 4e, f)** exhibited a coarse relief with signs of plastic elongation of titanium grains corresponding to the highest fracture toughness of the composite among the tested ones (Fig. 10b). No transgranular fracture across titanium grains occurred and no signs of debonding between Ti_5Si_3 phase grains or Ti_3SiC_2 MAX phase lamellae and titanium matrix were detected (**Fig. 4f**).

For composite 3, in contrast to composite 2, a temperature corresponding to the maximum of fracture toughness is about 800 °C (**Fig. 10b**). However, the shift by 200 °C compared to composite 1 is rather related to a difference in phase compositions of these materials. On fracture surface of a specimen of composite 3 tested at 700 °C (**Fig. 6e, f**), a coarse relief of fracture along titanium lamella packets with an average size smaller than in composite 2, with signs of plastic elongation of titanium grains, was observed. Such fracture surface morphology is consistent with slightly lower fracture toughness of composite 3 than composite 2 (**Fig. 10b**). Similarly to composite 2, no transgranular fracture across titanium grains was found and no signs of debonding between the $(Ti, Zr)_5Si_3$ or $TiC_{0.67}$ or Ti_3SiC_2 MAX phase components and the α-Ti matrix phase were detected (**Fig. 6f**).

In contrast to mechanical behavior of above-mentioned materials, composite 4 showed invariant values of both strength (**Fig. 10a**) and fracture toughness (**Fig. 10b**) in a temperature range of 20 °C to 600 °C. Strength of this composite is about 500 MPa in this temperature range with a trend to increasing, whereas fracture toughness is about 5 MPa·m$^{1/2}$. Increased strength (up to 650 MPa at 700 °C and 800 °C, **Fig. 10a**) and fracture toughness of the composite (steep increase up to 19 MPa·m$^{1/2}$ at 800 °C, **Fig. 10b**) are the evidences of a change in the fracture micromechanism. Fracture surface of a specimen of composite 4 undergone to the fracture toughness test at 20 °C showed signs of transgranular cleavage fracture with separation of fringe-like grain boundary regions of the chromium oxide, aluminum oxide, and Cr_2AlC phases and the titanium/chromium carbide phase particles in places where the advancing crack crossed them (**Fig. 8c, d**). A different pattern of fracture surface was observed in a specimen of composite 4 after the fracture toughness test at 700 °C (**Fig. 8e, f**). Because of intense plasticization of the Ti(Cr) matrix phase at this temperature, multiple microregions of ductile metal surrounding each of titanium/chromium carbide particles that are embodied into a Ti(Cr) matrix grains (**Fig. 8e**) with visible shear bands (**Fig. 8f**) as signs of plastic deformation of the matrix phase during crack growth can be seen. Such fracture micromechanism is related to a temperature-assisted relaxation of stress in the crack tip vicinity that corresponds to some increase in fracture toughness of the material at 700 °C (**Fig. 10b**). Finally, a phenomenon of substantial increase in both strength (**Fig. 10a**) and fracture toughness of the composite (**Fig. 10b**) at 800 °C may be explained in terms of phase transformations due to high-temperature diffusion of some elements, in particular, aluminum and oxygen [18, 52, 58, 102]. Besides, distinct "needle-shaped Cr_2AlC phase–Ti(Cr) matrix" interfaces disappeared due to the interdiffusion of chromium, aluminum, and oxygen between the chromium oxide phase, the Cr_2AlC MAX phase, and the matrix phase. This, in turn, caused a change in the fracture micromechanism [54, 75]. In this composite, high-temperature fracture occurred at 800 °C (**Fig. 8g, h**) with a steep increase in fracture toughness, due to diffusion of some elements and pore coalescence at the boundaries of the Ti(Cr) phase grains (**Fig. 8h**). No titanium/chromium carbide phase particles serve as stress concentrators, even in the places where the advancing crack crossed them (**Fig. 8g**). Thus, this temperature promotes quazi-ductile character of crack growth resulted in striations (**Fig. 8h**) similarly to fatigue crack growth in high-strength ductile materials at ambient temperature [54].

Thus, based on results of the strength test and fracture toughness tests along with analysis of microstructure peculiarities and fracture micromechanisms revealed in the whole temperature range investigated, the general tendencies in temperature dependent mechanical behavior of titanium-based composites have been

substantiated. The Ti–Si–X composites can serve as high-temperature structural materials at an operating temperature up to 750 °C, whereas the Ti–Cr–X composite exhibits high-temperature stability at a higher temperature by about 50 °C.

CONCLUSIONS

In this work, we have studied mechanical behaviors of the Ti–Si–X and Ti–Cr–X composites in a temperature range of 20–900 °C.

1. The microstructure peculiarities and phase compositions of the studied composites were substantiated.
2. It was shown that strength and fracture toughness parameters are suitable for the characterization of mechanical behavior of the composites in the investigated temperature range.
3. The phenomenon of increased strength and fracture toughness of Ti–Cr–Al–C composite was revealed and explained in terms of the morphology of microstructural components and dominant fracture micromechanisms.

Acknowledgments: The authors are thankful to the staff of the Scientific Equipment Collective Use Center "Laboratory of Advanced Technologies, Creation and Physicochemical Analysis of a New Substances and Functional Materials" at Lviv Polytechnic National University (https://lpnu.ua/ckkno) for their kind help in performing X-ray diffraction studies.

REFERENCES

1. D. Li, Y. Dong, Z. Zhang, Q. Zhang, S. Chen, N. Jia, H. Wang, B. Wang, K. Jin, Y. Xue, Y. Dou, X. He, W. Yang, L. Wang, H. Cai: Journal of Alloys and Compounds, 877, 2021, 160199. https://doi.org/10.1016/j.jallcom.2021.160199.
2. T. A. Prikhna, O. P. Ostash, A. S. Kuprin, V. Ya. Podhurska, T. B. Serbenyuk, E. S. Gevorkyan M. Rucki, W. Zurowski, W. Kucharczyk, V. B. Sverdun, M. V. Karpets, S. S. Ponomaryov, B. D. Vasyliv, V. E. Moshchil, M. A. Bortnitskaya: Composite Structures, 277, 2021, 114649. https://doi.org/10.1016/j.compstruct.2021.114649.
3. Z. Liu, J. Yang, Y. Qian, J. Xu, J. Zuo, M. Li: Ceramics International, 46, 2020, 22854–22860. https://doi.org/10.1016/j.ceramint.2020.06.055.
4. H. A. Shabri, M. H. D. Othman, M. A. Mohamed, T. A. Kurniawan, S. M. Jamil: Fuel Processing Technology, 212, 2021, 106626. https://doi.org/10.1016/j.fuproc.2020.106626.
5. T. B. Serbenyuk, T. O. Prikhna, V. B. Sverdun, N. V. Sverdun, V. Ye. Moshchil', O. P. Ostash, B. D. Vasyliv, V. Ya. Podhurska, V. V. Kovylyaev, V. I. Chasnyk: Journal of Superhard Materials, 40, 2018, 8–15. https://doi.org/10.3103/S1063457618010021.
6. L. A. Dobrzański, L. B. Dobrzański, A. D. Dobrzańska-Danikiewicz: Archives of Materials Science and Engineering, 102, 2020, 59–85. https://doi.org/10.5604/01.3001.0014.1525.
7. V. M. Posuvailo, V. V. Kulyk, Z. A. Duriagina, I. V. Koval'chuck, M. M. Student, B. D. Vasyliv: Archives of Materials Science and Engineering, 105, 2020, 49–55. https://doi.org/10.5604/01.3001.0014.5761.
8. T. S. Cherepova, H. P. Dmytrieva, O. I. Dukhota, M. V. Kindrachuk: Materials Science, 52, 2016, 173–179. https://doi.org/10.1007/s11003-016-9940-2.
9. M. H. Bocanegra-Bernal, S. Díaz de la Torre: Journal of Materials Science, 37, 2002, 4947–4971. https://doi.org/10.1023/A:1021099308957.
10. L. Ya. Ropyak, M. V. Makoviichuk, I. P. Shatskyi, I. M. Pritula, L. O. Gryn, V. O. Belyakovskyi: Functional Materials, 27, 2020, 638–642. https://doi.org/10.15407/fm27.03.638.
11. W. M. Budzianowski, J. Milewski: Recent Patents on Engineering, 5, 2011, 165–189. https://doi.org/10.2174/187221211797636926.
12. Y. Komatsu, A. Sciazko, N. Shikazono: Journal of Power Sources, 485, 2021, 229317. https://doi.org/10.1016/j.jpowsour.2020.229317.
13. E. B. Kashkarov, N. S. Pushilina, M. S. Syrtanov, D. G. Krotkevich, I. Gotman, N. Travitzky: Scripta Materialia, 194, 2021, 113696. https://doi.org/10.1016/j.scriptamat.2020.113696.
14. E. Tabares, S. C. Cifuentes, A. Jiménez-Morales, S. A. Tsipas: Powder Technology, 380, 2021, 96–105. https://doi.org/10.1016/j.powtec.2020.11.022.
15. S. N. Perevislov, T. V. Sokolova, V. L. Stolyarova: Materials Chemistry and Physics, 267, 2021, 124625. https://doi.org/10.1016/j.matchemphys.2021.124625.
16. L. Silvestroni, C. Melandri, J. Gonzalez-Julian: Journal of the European Ceramic Society, 41, 2021, 6064–6069. https://doi.org/10.1016/j.jeurceramsoc.2021.05.029.
17. Y. Tan, Y. Xia, Z. Teng, C. Chen, X. Zhou, H. Zhang: Journal of the European Ceramic Society, 41, 2021, 4658–4665. https://doi.org/10.1016/j.jeurceramsoc.2021.03.027.
18. W. Yu, X. Pi, W. Chen, M. Vallet, A. Guitton, L. Zhang: Materials Science and Engineering: A, 826, 2021, 141961. https://doi.org/10.1016/j.msea.2021.141961.
19. D. Yu, Y. Tan: Ceramics International, 47, 2021, 30188–30193. https://doi.org/10.1016/j.ceramint.2021.07.198.
20. T. Wejrzanowski, S. Haj Ibrahim, K. Cwieka, M. Loeffler, J. Milewski, E. Zschech, C.-G.Lee: Journal of Power Sources, 373, 2018, 85–94. https://doi.org/10.1016/j.jpowsour.2017.11.009.
21. V. Podhurska, B. Vasyliv: OMEE-2012: Proceedings, 2012, 293–294. https://doi.org/10.1109/OMEE.2012.6464761.
22. I. Danilenko, G. Lasko, I. Brykhanova, V. Burkhovetski, L. Ahkhozov: Nanoscale Research Letters, 12, 2017, 125. https://doi.org/10.1186/s11671-017-1901-7.
23. L. A. Dobrzański, L. B. Dobrzański, A. D. Dobrzańska-Danikiewicz: Journal of Achievements in Materials and Manufacturing Engineering, 99, 2020, 14–41. https://doi.org/10.5604/01.3001.0014.1598.
24. B. D. Vasyliv, V. Ya. Podhurska, O. P. Ostash, V. V. Vira: NANO 2017: Springer Proceedings in Physics, 214, 2018, 475–485. https://doi.org/10.1007/978-3-319-92567-7_30.
25. V. V. Kulyk, B. D. Vasyliv, Z. A. Duriagina, T. M. Kovbasiuk, I. A. Lemishka: Archives of Materials Science and Engineering, 108, 2021, 49–67. https://doi.org/10.5604/01.3001.0015.0254.
26. J. Milewski, J. Lewandowski, A. Miller: ASME Turbo Expo 2008: Proceedings, 2, 2008, 389–395. https://doi.org/10.1115/GT2008-50100.
27. J. Milewski, J. Lewandowski: Archives of Thermodynamics, 30, 2009, 3–12.
28. L. A. Dobrzański, L. B. Dobrzański, A. D. Dobrzańska-Danikiewicz: Journal of Achievements in Materials and Manufacturing Engineering, 98, 2020, 56–85. https://doi.org/10.5604/01.3001.0014.1481.
29. S. S. Savka, D. I. Popovych, A. S. Serednytski: NANO 2016: Springer Proceedings in Physics, 195, 2017, 145–156. https://doi.org/10.1007/978-3-319-56422-7_11.
30. J. Milewski, J. Kupecki, A. Szczęśniak, N. Uzunow: International Journal of Hydrogen Energy, 46, 2021, 35765–35776. https://doi.org/10.1016/j.ijhydene.2020.11.217.
31. B. Vasyliv, V. Podhurska, O. Ostash: Nanoscale Research Letters, 12, 2017, 265. https://doi.org/10.1186/s11671-017-2038-4

32. G. Witz, V. Shklover, W. Steurer, S. Bachegowda, H.-P. Bossmann: Journal of the American Ceramic Society, 90, 2007, 2935–2940.
https://doi.org/10.1111/j.1551-2916.2007.01785.x.
33. D. R. Clarke, C. G. Levi: Annual Review of Materials Research, 33, 2003, 383–417.
https://doi.org/10.1146/annurev.matsci.33.011403.113718.
34. M. Yu. Smyrnova-Zamkova, O. K. Ruban, O. I. Bykov, O. V. Dudnik: Composites Theory and Practice, 18, 2018, 234–240.
35. B. Vasyliv, J. Milewski, V. Podhurska, T. Wejrzanowski, V. Kulyk, J. Skibiński, V. Vira, Ł. Szabłowski, A. Szczęśniak, O. Dybiński: Applied Nanoscience, 2021.
https://doi.org/10.1007/s13204-021-01768-w.
36. M. Yu. Smyrnova-Zamkova, V. P. Red'ko, O. K. Ruban, O. V. Dudnik: Nanosistemi, Nanomateriali, Nanotehnologii, 15, 2017, 309–317.
https://doi.org/10.15407/nnn.15.02.0309.
37. O. V. Sukhova: Metallofizika i Noveishie Tekhnologii, 31, 2009, 1001–1012.
38. O. V. Dudnik, I. O. Marek, O. K. Ruban, V. P. Redko, M. I. Danilenko, S. A. Korniy, L. M. Melakh: Powder Metallurgy and Metal Ceramics, 59, 2020, 1–8.
https://doi.org/10.1007/s11106-020-00132-x.
39. V. G. Efremenko, Yu. G. Chabak, K. Shimizu, A. G. Lekatou, V. I. Zurnadzhy, A. E. Karantzalis, H. Halfa V. A. Mazur, B. V. Efremenko: Materials & Design, 126, 2017, 278–290.
https://doi.org/10.1016/j.matdes.2017.04.022.
40. X. W. Zhou, Y. F. Shen, H. M. Jin: Advanced Materials Research, 326, 2011, 151–156.
https://doi.org/10.4028/www.scientific.net/AMR.326.151.
41. A. V. Shevchenko, V. V. Lashneva, A. K. Ruban, V. V. Tsukrenko, E. V. Dudnik: Powder Metallurgy and Metal Ceramics, 54, 2016, 548–553.
https://doi.org/10.1007/s11106-016-9748-5.
42. M. Kujawa, R. Suwak, L. A. Dobrzański, A. Gerle, B. Tomiczek: Archives of Materials Science and Engineering, 107, 2021, 5–15.
https://doi.org/10.5604/01.3001.0014.8189.
43. I. O. Marek, O. K. Ruban, V. P. Redko, M. I. Danilenko, S. A. Korniy, O. V. Dudnik: Powder Metallurgy and Metal Ceramics, 58, 2019, 125–132.
https://doi.org/10.1007/s11106-019-00055-2.
44. F. W. Crossman, A. S. Yue: Metallurgical Transactions, 2, 1971, 1545–1555.
45. H. Zhao, L. Hu, C. Li, Q. Jiao, J. He, Y. Qin, F. Yin: Ceramics International, 47, 2021, 17570–17579.
https://doi.org/10.1016/j.ceramint.2021.03.075.
46. W.-T. Chiu, K. Wakabayashi, A. Umise, M. Tahara, T. Inamura, H. Hosoda: Journal of the Mechanical Behavior of Biomedical Materials, 123, 2021, 104707.
https://doi.org/10.1016/j.jmbbm.2021.104707.
47. A. Kehal, N. Saoula, S.-E.-H. Abaidia, C. Nouveau: Surface and Coatings Technology, 421, 2021, 127444.
https://doi.org/10.1016/j.surfcoat.2021.127444.
48. W. T. Chiu, T. Ishigaki, N. Nohira, A. Umise, M. Tahara, T. Inamura, H. Hosoda: Journal of Alloys and Compounds, 867, 2021, 159037.
https://doi.org/10.1016/j.jallcom.2021.159037.
49. W.-T. Chiu, K. Wakabayashi, A. Umise, M. Tahara, T. Inamura, H. Hosoda: Journal of Alloys and Compounds, 875, 2021, 160088.
https://doi.org/10.1016/j.jallcom.2021.160088.
50. X. Zhao, M. Sokol, M. W. Barsoum, L. Lamberson: Materials Science and Engineering: A, 809, 2021, 140869.
https://doi.org/10.1016/j.msea.2021.140869.
51. T. Prikhna, O. Ostash, T. Basyuk, A. Ivasyshyn, V. Sverdun, M. Loshak, S. Dub, V. Podgurska, V. Moshchil, T. Cabioc'h, P. Chartier, M. Karpets, V. Kovylaev, O. Starostina, A. Kozyrev: Solid State Phenomena, 230, 2015, 140–143.
https://doi.org/10.4028/www.scientific.net/SSP.230.140.
52. Z. Zhang, X. Duan, D. Jia, Y. Zhou, S. van der Zwaag: Journal of the European Ceramic Society, 41, 2021, 3851–3878.
https://doi.org/10.1016/j.jeurceramsoc.2021.02.002.
53. A. Ivasyshyn, O. Ostash, T. Prikhna, V. Podhurska, T. Basyuk: Nanoscale Research Letters, 11, 2016, 358.
https://doi.org/10.1186/s11671-016-1571-x.
54. O.P. Ostash, A. D. Ivasyshyn, B. D. Vasyliv, I. Yu. Okun': Materials Science, 42, 2006, 330–343.
https://doi.org/10.1007/s11003-006-0087-4.
55. A. Shylo, A. Doroshkevich, A. Lyubchyk, Y. Bacherikov, M. Balasoiu, T. Konstantinova: Applied Nanoscience, 10, 2020, 4395–4402.
https://doi.org/10.1007/s13204-020-01471-2.
56. G. Frommeyer, R. Rosenkranz, C. Ludecke: International Journal of Materials Research, 81, 1990, 307–313.
https://doi.org/10.1515/ijmr-1990-810501
57. M. W. Barsoum: Progress in Solid State Chemistry, 28, 2000, 201–281.
https://doi.org/10.1016/S0079-6786(00)00006-6.
58. R. Liu, M. Tane, H. Kimizuka, Y. Shirakami, K.-i. Ikeda, S. Miura, K. Morita, T. S. Suzuki, Y. Sakka, L. Zhang, T. Sekino: Journal of the European Ceramic Society, 41, 2021, 2278–2289.
https://doi.org/10.1016/j.jeurceramsoc.2020.11.026.
59. M. S. Park, W.-T. Chiu, N. Nohira, M. Tahara, H. Hosoda: Materials Science and Engineering: A, 822, 2021, 141668.
https://doi.org/10.1016/j.msea.2021.141668.
60. K. H. Omran, M. S. Abd El-sadek, M. Mostafa, O. M. Hemeda: Applied Nanoscience, 10, 2020, 2315–2327.
https://doi.org/10.1007/s13204-020-01390-2.
61. V. I. Mazur, Y. N. Taran, S. V. Kapustnikova et al (1994) Titanium matrix composites. US Patent, No. 5366570, 22.11.1994
62. B. Vasyliv, A. Ivasyshyn, O. Ostash, S. Firstov, V. Mazur, M. Kuzmenko, S. Kapustnikova: Metallic Materials with High Structural Efficiency: Part of the NATO Science Series II: Mathematics, Physics and Chemistry, 2004, 235–240.
https://link.springer.com/chapter/10.1007/1-4020-2112-7_24.
63. B. D. Vasyliv, A. D. Ivasyshyn, O. P. Ostash, V. I. Mazur: Materials Science, 38, 2002, 220–224.
https://doi.org/10.1023/A:1020990103898.
64. O. P. Ostash, A. D. Ivasyshyn, B. D. Vasyliv, V. I. Mazur, S. V. Kapustnikova: Materials Science, 38, 2002, 55–61.
https://doi.org/10.1023/A:1020120714703.
65. A. S. Doroshkevich, E. B. Asgerov, A. V. Shylo, A. I. Lyubchyk, A. I. Logunov, V. A. Glazunova, A. Kh. Islamov, V. A. Turchenko, V. Almasan, D. Lazar, M. Balasoiu, V. S. Doroshkevich, A. I. Madadzada, Kh. T. Kholmurodov, V. I. Bodnarchuk, B. L. Oksengendler: Applied Nanoscience, 9, 2019, 1603–1609.
https://doi.org/10.1007/s13204-019-00979-6.
66. K.-W. Jeong, J.-S. Han, G.-U. Yang, D.-J. Kim: Materials, 14, 2021, 2767.
https://doi.org/10.3390/ma14112767.
67. A. I. Yurkova, S. O. Nakonechnyi, V. V. Cherniavsky, V. V. Kushnir: Applied Nanoscience, 2021.
https://doi.org/10.1007/s13204-021-01856-x.
68. R. N. Gupta: Applied Nanoscience, 11, 2021, 173–185.
https://doi.org/10.1007/s13204-020-01567-9.
69. S. Tao, J. Yang, M. Zhai, F. Shao, X. Zhong, H. Zhao, Y. Zhuang, J. Ni, W. Li, S. Tao: Crystals, 10, 2020, 984.
https://doi.org/10.3390/cryst10110984.
70. V. Y. Podhurs'ka, B. D. Vasyliv, O. P. Ostash, O. D. Vasyl'ev, E. M. Brodnikovs'kyi: Materials Science, 49, 2014, 805–811.

https://doi.org/10.1007/s11003-014-9677-8.
71. A. B. Hernandez, D. Cortés-Arriagada, H. Camacho García, E. Chigo Anota, M. Salazar Villanueva: Applied Nanoscience, 10, 2020, 37–49.
https://doi.org/10.1007/s13204-019-01072-8.
72. O. V. Perlova, Yu. S. Dzyazko, A. V. Palchik, I. S. Ivanova, N. O. Perlova, M. O. Danilov, I. A. Rusetskii, G. Ya. Kolbasov, A. G. Dzyazko: Applied Nanoscience, 10, 2020, 4591–4602.
https://doi.org/10.1007/s13204-020-01313-1.
73. A. S. Basaleh, R. M. Mohamed: Applied Nanoscience, 9, 2019, 2051–2058.
https://doi.org/10.1007/s13204-019-00992-9.
74. A. Sciazko, T. Shimura, Y. Komatsu, N. Shikazono: Journal of Thermal Science and Technology, 16, 2021, JTST0013.
https://doi.org/10.1299/jtst.2021jtst0013.
75. O. M. Romaniv, B. D. Vasyliv: Materials Science, 34, 1998, 149–161.
https://doi.org/10.1007/BF02355530.
76. V. G. Efremenko, Y. G. Chabak, A. Lekatou, A. E. Karantzalis, A. V. Efremenko: Metallurgical and Materials Transactions A, 47, 2016, 1529–1543.
https://doi.org/10.1007/s11661-016-3336-7.
77. S. Buchaniec, A. Sciazko, M. Mozdzierz, G. Brus: IEEE Access, 7, 2019, 34361–34372.
https://doi.org/10.1109/ACCESS.2019.2904327.
78. O. M. Romaniv, I.V. Zalite, V. M. Simin'kovych, O. N. Tkach, B. D. Vasyliv: Materials Science, 31, 1996, 588–594.
https://doi.org/10.1007/BF00558793.
79. P. Khajavi, P. V. Hendriksen, J. Chevalier, L. Gremillard, H. L. Frandsen: Journal of the European Ceramic Society, 40, 2020, 5670–5682.
https://doi.org/10.1016/j.jeurceramsoc.2020.05.042.
80. A. D. Ivasyshyn, B. D. Vasyliv: Materials Science, 37, 2001, 1002–1004.
https://doi.org/10.1023/A:1015669913601.
81. B. D. Vasyliv: Materials Science, 38, 2002, 724–728.
https://doi.org/10.1023/A:1024222709514.
82. R. F. Cook, G. M. Pharr: Journal of the American Ceramic Society, 73, 1990, 787–817.
https://doi.org/10.1111/j.1151-2916.1990.tb05119.x.
83. A. Nastic, A. Merati, M. Bielawski, M. Bolduc, O. Fakolujo, M. Nganbe: Journal of Materials Science & Technology, 31, 2015, 773–783.
https://doi.org/10.1016/j.jmst.2015.06.005.
84. Z. Duriagina, V. Kulyk, T. Kovbasiuk, B. Vasyliv, A. Kostryzhev: Metals, 11, 2021, 434.
https://doi.org/10.3390/met11030434.
85. ASTM E 384-11 Standard test method for Knoop and Vickers hardness of materials, ASTM International, 2011.
https://doi.org/10.1520/E0384-11.
86. ASTM C 1327-03 Standard test method for Vickers indentation hardness of advanced ceramics, ASTM International, 2003.
https://doi.org/10.1520/C1327-03.
87. B. R. Lawn, M. V. Swain: Journal of Materials Science, 10, 1975, 113–122.
https://doi.org/10.1007/BF00541038.
88. G. A. Gogotsi, S. N. Dub, E. E. Lomonova, B. I. Ozersky: Journal of the European Ceramic Society, 15, 1995, 405–413.
https://doi.org/10.1016/0955-2219(95)91431-M.
89. A. G. Evans, E. A. Charles: Journal of the American Ceramic Society, 59, 1976, 371–372.
https://doi.org/10.1111/j.1151-2916.1976.tb10991.x.
90. O. N. Grigoriev, V. B. Vinokurov, T. V. Mosina, L. M. Melakh, N. D. Bega, A. V. Koroteev, L. I. Klimenko, A. V. Stepanenko: Powder Metallurgy and Metal Ceramics, 55, 2017, 676–688.
https://doi.org/10.1007/s11106-017-9855-y.
91. G. R. Anstis, P. Chantikul, B. R. Lawn, D. B. Marshall: Journal of the American Ceramic Society, 64, 1981, 533–538.
https://doi.org/10.1111/j.1151-2916.1981.tb10320.x.
92. I. Danilenko, F. Glazunov, T. Konstantinova, I. Yashchyshyn, V. Burkhovetski, G. Volkova: Advanced Materials Letters, 5, 2014, 465–471.
https://doi.org/10.5185/amlett.2014.amwc1040II.
93. B. R. Lawn, A. G. Evans, D. B. Marshall: Journal of the American Ceramic Society, 63, 1980, 574–581.
https://doi.org/10.1111/j.1151-2916.1980.tb10768.x.
94. M. Y. Smyrnova-Zamkova, O. K. Ruban, O. I. Bykov, M. Ya. Holovchuk, T. V. Mosina, O. I. Khomenko, E. V. Dudnik: Powder Metallurgy and Metal Ceramics, 60, 2021, 129–141.
https://doi.org/10.1007/s11106-021-00222-4.
95. J. Lankford: Journal of Materials Science Letters, 1, 1982, 493–495.
https://doi.org/10.1007/BF00721938.
96. B. Vasyliv, V. Kulyk, Z. Duriagina, D. Mierzwinski, T. Kovbasiuk, T. Tepla: Eastern-European Journal of Enterprise Technologies, 6, 2020, 67–77.
https://doi.org/10.15587/1729-4061.2020.218291.
97. V. V. Kulyk, Z. A. Duriagina, B. D. Vasyliv, V. Vavrukh, T. M. Kovbasiuk, M. Holovchuk: Archives of Materials Science and Engineering 109, 2021, 65–79.
https://doi.org/10.5604/01.3001.0015.2625.
98. ASTM E 399-20a Standard test method for linear-elastic plane-strain fracture toughness of metallic materials, ASTM International, 2020.
https://doi.org/10.1520/E0399-20A.
99. ASTM C 1421-18 Standard test methods for determination of fracture toughness of advanced ceramics at ambient temperature, ASTM International, 2018.
https://doi.org/10.1520/C1421-18.
100. J. Kübier: From a preliminary study to a standard test method, in Fracture Resistance Testing of Monolithic and Composite Brittle Materials, ASTM International, 2002, 93–106.
https://doi.org/10.1520/STP10473S.
101. L. Akselrud, Y. Grin: Journal of Applied Crystallography, 47, 2014, 803–805.
https://doi.org/10.1107/S1600576714001058.
102. Z. Wang, G. Ma, L. Liu, L. Wang, P. Ke, Q. Xue, A. Wang: Corrosion Science, 167, 2020, 108492.
https://doi.org/10.1016/j.corsci.2020.108492.